Journal of Materials Chemistry A

ROYAL SOCIETY OF CHEMISTRY

PAPER

View Article Online
View Journal | View Issue

Cite this: J. Mater. Chem. A, 2021, 9, 14928

Atomistic understanding of the $LiNiO_2$–NiO_2 phase diagram from experimentally guided lattice models†

Markus Mock,‡[a] Matteo Bianchini, ‡[ab] François Fauth, [c] Karsten Albe [d] and Sabrina Sicolo *[a]

The compositional phase diagram of $LiNiO_2$ as a function of lithium content has been the object of numerous experimental and computational studies over the last two decades. Even between experimental studies, inconsistencies emerge on the position, width, and the very existence of single- and two-phase fields. Modelling of the phase diagram has always been a daunting task and resulted in the prediction of several stable Li phases that were not observed experimentally. Aiming at resolving the sources of discrepancy among experiments and between experiments and theory, we combine *operando* X-ray diffraction and Rietveld refinement with Monte Carlo simulations using a modified cluster expansion formalism at the Density Functional Theory (DFT) level. A surrogate lattice model pinpoints the influence of off-stoichiometry and elemental substitution on the phase diagram and phase transitions and yields an unprecedented match to experimental phase diagrams. We conclude that the first and foremost effect of both off-stoichiometry and elemental substitution is to disrupt Li ordering, suppress phase transitions and promote solid-solution behavior and the corresponding smoothing of discharge curves. Our model is particularly effective at reproducing the monoclinic domain and allows to draw a correspondence between electrochemical features (d|x|/dV curve) and Li-vacancy orderings (including the first identification of a $Li_{5/8}NiO_2$ structure). Deviations from experiments at both ends of the phase diagram are resolved and attributed to faulting (at high state of charge) and sluggish kinetics (at low state of charge).

Received 20th January 2021
Accepted 7th June 2021

DOI: 10.1039/d1ta00563d

rsc.li/materials-a

1 Introduction

Layered oxides are the most popular cathode active materials for Li-ion batteries. $LiCoO_2$ in particular is the material of choice in the electronics industry.[1] However, the increasing human, environmental and financial cost of cobalt spells out the need for cobalt-free cathode active materials, especially for automotive applications.[2,3] For nearly three decades, the isostructural compound $LiNiO_2$ (LNO) has been in the spotlight as a substitute of $LiCoO_2$ due to its same high theoretical capacity at a lower cost.[4,5] Unfortunately, the material is afflicted by mechanical and thermodynamic instabilities[6] that have prevented its commercialization. Nevertheless, as the Li-ion market is evolving towards cathodes with ever increasing Ni content, LNO is a useful and apparently simple model system that however is not fully understood yet.

During electrochemical cycling of LNO several phases appear, conventionally labelled by their crystallographic symmetry:[5,7–11] H1 → M → H2 → H3 upon charge (delithiation). Here H stands for hexagonal ($R\bar{3}m$ space group) and M for monoclinic ($C2/m$ space group). In the notation of Delmas *et al.*,[12] all the H phases are three-layered O3 phases (ABCABC oxygen stacking). A phase labeled H4, with O1 stacking, has also been reported for extremely delitiathed compositions close to NiO_2, but it is not observed under typical experimental conditions.[13] All these single phases are separated by two-phase regions corresponding to first-order phase transitions. From a computational point of view, the phase diagram of $LiNiO_2$ has been studied within the cluster expansion formalism since 2002.[14–16] Early studies[14,15] focused on the topotactic delithiation of $LiNiO_2$ and presented notable Li-vacancy orderings stabilized as a function of Li content. A recent study[16] provides a more sophisticated mapping strategy and addresses the ternary phase diagram of the (Li–Ni-vacancy)–O system to study densification triggered by oxygen loss, another significant challenge of all Ni-

[a]BASF SE, Carl-Bosch-Strasse 38, 67056 Ludwigshafen am Rhein, Germany. E-mail: sabrina.sicolo@basf.com

[b]Battery and Electrochemistry Laboratory, Institute of Nanotechnology, Karlsruhe Institute of Technology (KIT), Hermann-von-Helmholtz-Platz 1, 76344 Eggenstein-Leopoldshafen, Germany

[c]CELLS – ALBA Synchrotron, Cerdanyola del Vallés, 08290 Barcelona, Spain

[d]Technische Universität Darmstadt, Institut für Materialwissenschaft, Fachgebiet Materialmodellierung, Otto-Berndt-Str. 3, 64287 Darmstadt, Germany

† Electronic supplementary information (ESI) available. See DOI: 10.1039/d1ta00563d

‡ These authors contributed equally to this work.

rich CAMs. In LNO, in particular, oxygen loss occurs at high state of charge (low Li content) in correspondence with the H2 and especially H3 phases, leading to surface densification toward a rock salt-type structure and ultimately to reduced electrochemical performances.[7,17,18]

Fig. 1 compares experimental and calculated compositional phase diagrams as a function of lithium content obtained over the last two decades. It is apparent that some discrepancies exist on the positions and widths of both one- and two-phase fields. For the earlier *in situ* studies, this can be easily explained because low capacity was accessed.[10] The existence and width of the M phase region has also been debated, since such phase is not observed in samples with too large an off-stoichiometry (z > 7%).[6] The most striking discrepancy between experiments and calculations[14] is the prediction of several stable Li phases in the M region that have never been experimentally observed. In general, less attention has been paid to the discrepancies at lower Li content, which nowadays can be experimentally accessed more reproducibly than in the past. Even between recent investigations there is no consensus on the compositional range attributed to the H2, H3 and H2/H3 domains. Yet, the behavior in the charged (delithiated) state is crucial to the performance of the material: delithiation is accompanied by severe volume shrinkage, largely due to the H2/H3 transition that alone entails a volume change of about 4–5%.[7] The coexistence of phases having dramatically different volumes leads to interfacial strain, which is then released in the form of cracking in the primary and secondary particles.[17]

Even synthesis poses a challenge, in that LNO exhibits a strong tendency toward off-stoichiometry in the form of $Li_{1-z}Ni_{1+z}O_2$ (z = 1% to 2%).[19,20] Keeping in mind the strong correlation between Li mobility in layered oxides and the size of the Li interlayer[21] and the fact that Ni^{2+} is a smaller cation than Li^+, excess Ni is detrimental for the electrochemical performance of LNO. It has been suggested that the oxidation of Ni^{2+} to the even smaller Ni^{3+} upon charging causes an irreversible local collapse of the interslab space, kinetically preventing the re-intercalation of Li during discharge.[20] Each extra Ni in the Li layer ($Ni^{\cdot}_{Li}$ in Kröger–Vink notation, here Ni_{Li} for simplicity) might effectively block re-intercalation into its six nearest-neighbor Li sites (Fig. 2a), as confirmed also by *ab initio* molecular dynamics simulations.[22]

The drawbacks of LNO are often overcome by elemental substitution strategies, leading to the synthesis and commercialization of isostructural oxides, named lithium nickel-cobalt-manganese (NCM) and lithium nickel-cobalt-aluminum (NCA) oxides.[23–25] Despite the lower discharge specific capacity due to the redox inactivity of Al^{3+} and Mn^{4+}, Ni substitution largely improves structural and thermal stability, resulting in a smoothing of voltage curves and the suppression of the multiple phase transitions.[26,27] Being both isovalent with Ni^{3+} and redox active, Co does not affect the capacity of $LiNiO_2$, but Al, Mn, and Mg all have an impact. Al^{3+} is not electrochemically active, automatically hindering the deintercalation of an equivalent amount of Li (Fig. 2b). Moreover, Al increases the average voltage due to greater covalency of the Al–O bond with respect to Ni–O.[28] The case of Mn^{4+} is more complex as it concurrently lowers the average Ni oxidation state, thereby increasing the presence of Ni^{2+} in the Li layer.[27] Mg^{2+} is yet a different scenario as it appears to substitute Li rather than Ni depending on the Mg concentration.[29]

Overall, the impact of substituents on the properties of LNO is a non-trivial superposition of various factors, whose quantification certainly requires an ad-hoc study for each substituent. Nevertheless, we will demonstrate that a surrogate lattice model is able to account for the main effect of Ni off-stoichiometry and

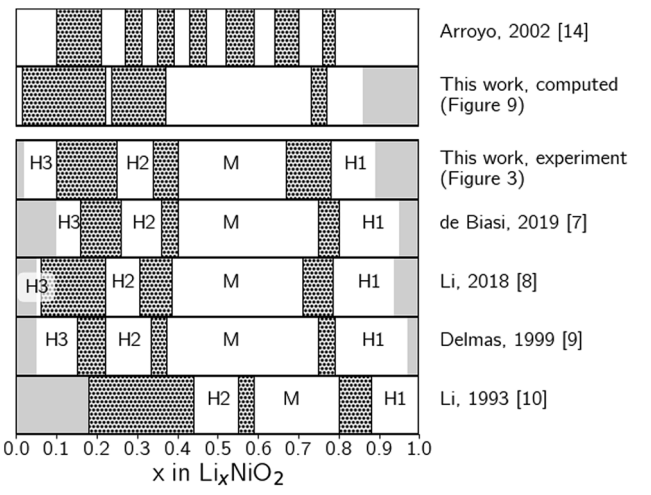

Fig. 1 Comparison between experimental phase diagrams obtained from *in situ* X-ray diffraction experiments[7–10] and *ab initio* simulations.[14] Results from this work are also shown, as a preview of following sections. Single- and two-phase regions are depicted as white and hatched areas, respectively. Solid light grey areas represent compositions inaccessible after the first cycle.

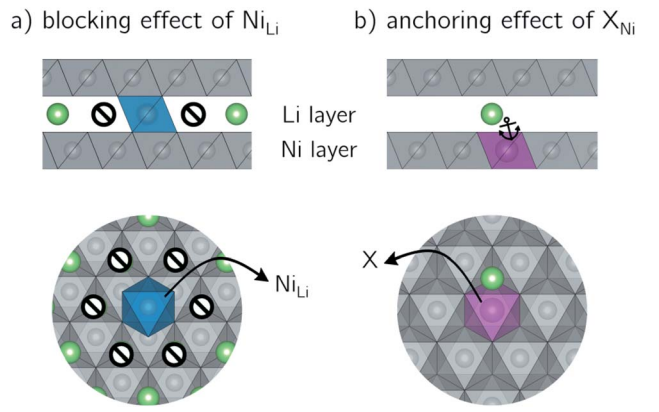

Fig. 2 Schematic representation of the effect of substituents on the Li (a) and Ni (b) sublattices. In (a) the element can be Ni_{Li} to exemplify the case of off-stoichiometry. Ni_{Li} effectively blocks seven Li sites in hexagonal arrangement; (b) a redox-inactive substituent on the Ni site hinders the deintercalation of a Li^+ ion by "anchoring" it. Li^+ ions and NiO_6 octahedra are pictured as green spheres and grey polyhedra, respectively; an extra Ni in the Li layer is represented by a blue octahedron, whereas a Ni substituent "X" is shown in purple. Side and top views are shown.

substitution, namely the disruption of Li ordering by either forced Li depletion (as is the case for Ni_{Li}, Fig. 2a) or forced Li occupancy, or "anchoring" (as is the case for certain dopants, Fig. 2b).

In this work, we employ a joint experimental and computational approach that combines *operando* X-ray diffraction and Rietveld refinement with the cluster expansion formalism at the Density Functional Theory (DFT) level. By doing so, we explicitly address the sources of discrepancy among experiments and between experiments and theory, the effect of off-stoichiometry and elemental substitution on the phase diagram and the features of the various Li-vacancy orderings and phase transitions.

2 Methods

2.1 Computational approach

Spin-polarized calculations in the framework of DFT have been performed using the Vienna *ab initio* Simulation Package (VASP)[30–33] with projector augmented wave pseudopotentials.[34,35] The exchange-correlation functional of choice is the strongly constrained and appropriately normed (SCAN) meta-generalized gradient approximation supplemented with the long-range van der Waals interaction from rVV10, the revised Vydrov–van Voorhis nonlocal correlation functional, which has been proven to perform excellently on layered materials.[36] SCAN's reliability against other popular functionals has already been established by Chakraborty;[37] a benchmark of SCAN-rVV10 with respect to SCAN-rVV10+U, PBE-D3+U and HSE06 can be found in the ESI (Fig. S1†). All structures have been fully relaxed with a cutoff energy of 600 eV and a k-point spacing of 0.25 $Å^{-1}$ until the forces were lower than 0.01 eV $Å^{-1}$.

The properties calculated with the DFT calculations were used to construct a lattice model based on the cluster expansion (CE) method.[38,39] Within the cluster expansion formalism, the variation of the property of interest Q with site occupancy σ is expanded as a set for cluster functions Φ_α:

$$Q(\sigma) = Q_0 + \sum_\alpha \Phi_\alpha m_\alpha J_\alpha, \quad (1)$$

where m_α is the multiplicity of cluster α, and the effective cluster interactions J_α are the free parameters of the CE and target of the fitting procedure.

When the property of interest is the formation energy of a compound, the cluster expansion technique paves the way for the construction of compositional phase diagrams *via* the convex hull formalism, as it has been done in the past for many popular intercalation compounds such as $LiNiO_2$,[14–16] $LiCoO_2$ (ref. 40 and 41) and $Li(Ni_{0.5}Mn_{0.5})O_2$.[42] The convex hull represents phase stability as a function of composition, accounting for all possible decomposition paths. It is important to remark that the convex hull calculated from DFT energies at 0 Kelvin does not include entropy contributions. Conclusions about phase stability can only be drawn after including finite temperature effects. One of the perks of the cluster expansion formalism is its ability to capture configurational entropy contributions, which are likely significant when studying lattice occupancies. Although we are neglecting vibrational entropy, we work under the approximation that its variation across the compositional space of the same compound is small relative to the configurational energy and entropy and thus does not affect the relative phase stabilities.[43]

The CE was constructed using the software package ICET,[44] based on a database of 499 structures with varying Li content, containing 4 to 56 lattice sites. The database of structures was generated augmenting a simple enumeration scheme with the recursive use of intermediate cluster expansions to identify new promising configurations. The final cluster expansion was constructed using cutoffs of 8.5966 Å, 8.1068 Å and 6.4169 Å for pair, triplet and quadruplet interactions.

We calculated the compositional phase diagram of Li_xNiO_2 performing Monte Carlo simulations in the semi-grand canonical ensemble—*i.e.*, at constant temperature T, total number of sites N and chemical potential difference $\Delta\mu$ between vacancies and Li ions—with the aid of the mchammer module of ICET.[44] Simulations were started at 2000 K and equally spaced chemical potential differences between −0.6 eV per f.u. to 0.6 eV per f.u. The temperature was reduced in steps of 50 K until 0 K; at every temperature, the resulting concentration was equilibrated using the algorithm proposed by van de Walle and Asta[45] and the final configuration was used to initialize a new simulation at the following temperature. The resulting isochemical potential lines gather in one-phase regions and outline two-phase fields as gaps, allowing for the calculation of phase diagrams.

A conceptual hurdle emerged when computing phase diagrams as a function of the system size. It is a well-known sanity check that the energetics of atomic orderings converge with increasing system sizes. It was then unexpected that shape effects, too, would arise due to the (in)ability of a supercell to accommodate different atomic arrangements (Fig. S2 and S3†). To correctly compare the stabilities of different orderings, we calculated each configuration in an appropriately shaped supercell and generated a composite phase diagram (Fig. 5a).

2.2 Experimental procedures

$LiNiO_2$ was synthesized with a solid-state approach as described elsewhere.[7] Briefly, $LiOH \cdot H_2O$ and $Ni(OH)_2$ (BASF SE) precursors were mixed in a 1.01 Li/Ni molar ratio and calcined in O_2 at 700 °C for 6 h. A Li-deficient sample was also prepared under the same conditions by reducing the Li/Ni molar ratio to 0.99. $LiNi_{0.95}Al_{0.05}O_2$ was synthesized analogously from a mixed metal hydroxide precursor $Ni_{0.95}Al_{0.05}(OH)_2$ (BASF SE) at 750 °C for 12 h. The samples were moved to an Ar-filled glovebox immediately after synthesis and sieved with a 45 μm sieve. The crystal structure of the samples was verified by XRD in Debye-Sherrer geometry. Al-doped LNO and Li-deficient LNO were measured in house with Cu $K_{\alpha 1}$ radiation, while stoichiometric LNO (nominal Li/Ni ratio 1.01) was measured with synchrotron radiation (beamline parameters as described for the *operando* experiment below). The samples were loaded in a glass capillary (0.3 and 0.5 mm diameter for the in house and synchrotron measurements, respectively).

Cathodes were prepared by slurry casting onto Al foil. The slurry was obtained by dispersing 94 wt% LNO, 3 wt% Super C65 carbon black (Timcal), and 3 wt% Solef polyvinylidene fluoride binder (Solvay) in N-methyl-2-pyrrolidone. For regular electrochemical testing, half coin half cells were assembled inside an Ar-filled glovebox. These consisted of cathode ($\approx$6 mg cm^{-2}), GF/A glass microfiber separator (GE Healthcare Life Sciences), and Li metal anode (Albemarle Germany GmbH) with diameters of 13, 17, and 15 mm, respectively, using 95 μL of LP57 electrolyte (1 M $LiPF_6$ in 3 : 7 by weight ethylene carbonate and ethyl methyl carbonate; BASF SE). Galvanostatic cycling was performed in the voltage range between 3.0 and 4.3 V *vs.* Li^+/Li at C/20 (1C = 225 mA g^{-1}). For *operando* XRD, pouch half-cells were assembled inside a dry room with dew point below −50 °C. The cathode was stacked on Celgard 2500 polypropylene separator and lithium foil anode, using 250 μL of LP57 as electrolyte. The pouch cell was mounted on the diffractometer at the MSPD beamline[46] of the ALBA synchrotron. We measured *operando* the second discharge: the first cycle and the second charge were conducted at a rate of C/10 between 3 V and 4.3 V. The voltage was then hold at 4.3 V for four hours to reach nearly full-charge state ($x = 0.02$), prior to the second discharge, which was done slowly at C/20 rate while measuring synchrotron XRD patterns continuously at 25 °C (Fig. S4†). We recorded one XRD pattern every 260 s, *i.e.* $\Delta x = 0.003$ Li between subsequent patterns. The pouch cell was measured in transmission geometry, with the beam going through all the layers of the cell. The operating wavelength was $\lambda = 0.61953(3)$ nm as refined using a NIST standard silicon sample (NIST SI640D). Powder diffraction patterns were collected using the one-dimensional silicon based position sensitive detector MYTHEN in the 2–53° 2θ angular range. Since MYTHEN detector spans a 40° angular 2θ range, this setup allows fast data acquisition with extremely high statistics and good angular resolution, allowing Rietveld structural refinements of all the identified phases using the Fullprof software.[47] For the refinement, unit cell parameters and phase fractions of each phase were always refined, while peak shapes, oxygen z coordinates and Debye-Waller factors were refined in single-phase fields and fixed in two-phase ones. An additional Al phase (due to the Al present in the pouch foil and in the positive current collector) was added in the refinement and treated with a LeBail whole pattern fitting. Diffraction patterns exhibiting stacking faults were simulated with the FAULTS software.[48]

3 Results

3.1 *Operando* synchrotron X-ray diffraction

We begin by re-investigating the electrochemical behavior of LNO in real time. We employ *operando* synchrotron XRD aiming for high angular and time resolution. We focus on the second discharge, carried out in an unmodified pouch cell at low current rate (C/20) to obtain reliable electrochemical performances and high compositional resolution ($\Delta x = 0.003$ between XRD patterns). The employed LNO had the expected rhombohedral crystal structure in the pristine state, with $z = 2.4(1)$% Ni in the Li site (Table S1†). Fig. 3a shows the *operando* synchrotron XRD data, confirming the typical behavior reported in the literature: H3 → H2 → M → H1 during discharge. Rietveld refinement of the data (as exemplified in Fig. S5†) allows to obtain phase fractions and accurate cell parameters (Fig. 3b). In general, we find a rather good agreement with recently reported data.[7,8] The H3 solubility domain extends from nearly complete delithiation (0.02) to $x = 0.11$. As expected, we do not observe any H4 phase, which would only appear when no lithium remains in the NiO_2 structure. H2 instead is found between $x = 0.25$ and 0.34, while the monoclinic domain extends from 0.4 to 0.67. Although an explanation for its existence has been suggested for the domain $0.5 < x < 0.75$ due to peculiar Li/vacancy orderings,[49] it is not sufficient to fully represent the experimental data since all authors (Fig. 1) agree on the M domain extending to 0.4 (*i.e.* well beyond 0.5). Remarkably, 0.4 would agree with a computationally-predicted stable phase at $x = 2/5$.[14,15] Finally, we observe H1 in the composition range $0.78 < x < 0.9$. Full lithiation is normally not achieved after the first charge due to poor kinetics in this domain, as we will also discuss later.[8,24] Fig. 3b also gathers the unit cell parameters obtained from refinement. The oxygen atomic coordinate z_O and Debye–Waller factors were also refined in the single-phase domains and fixed in the two-phase ones (Fig. S6†). The behavior of the unit cell parameters a and c is as expected.[6] However, we shall note the striking difference in the H3 phase unit cell volume between our data and the recent ones of Li *et al.*[8] and de Biasi *et al.*[7] Due to our experimental conditions, we are able to deeply delithiate LNO and obtain a very Li-poor H3 phase, hence with a much smaller unit cell volume. The volume of H3 clearly varies before H2 appears, thus reinforcing the hypothesis that H3 is not a single phase but instead a domain with variable Li content. Finally, while the volumes of H1, M and H2 phases agree well between different authors, that is not the case for H3. The H2–H3 relative volume change in the two-phase region can vary from 3.8% (de Biasi *et al.*[7]) to 5.3% in our case. This discrepancy can be partially due to experimental conditions, and partially to the fact that well-stoichiometric LNO is more likely to reach nearly full delithiation, thus larger volume variation.[6]

Keeping in mind our experimental observations, and especially the discrepancies between different experiments, we undertake an *ab initio* investigation of the phase diagram of LNO based on the DFT-computed convex hull and on the cluster expansion method.

3.2 Cluster expansion formalism

When addressing the delithiation of $LiNiO_2$, the formation energy of a given phase Li_xNiO_2 is calculated from its total energy and the energies of the reference compounds, $LiNiO_2$ and NiO_2:

$$E_f = E_{LixNiO2} - x \cdot E_{LixNiO2} - (1 - x) \cdot E_{NiO2} \quad (2)$$

It is apparent that the formation energy of a compound—and thus the shape of the convex hull and in turn of the phase diagram—depends heavily on the knowledge of the end-members and their total energies. Choosing the wrong ground states results in skewed comparisons with experimental data. In particular for the lithiated compound, this choice is not trivial, in

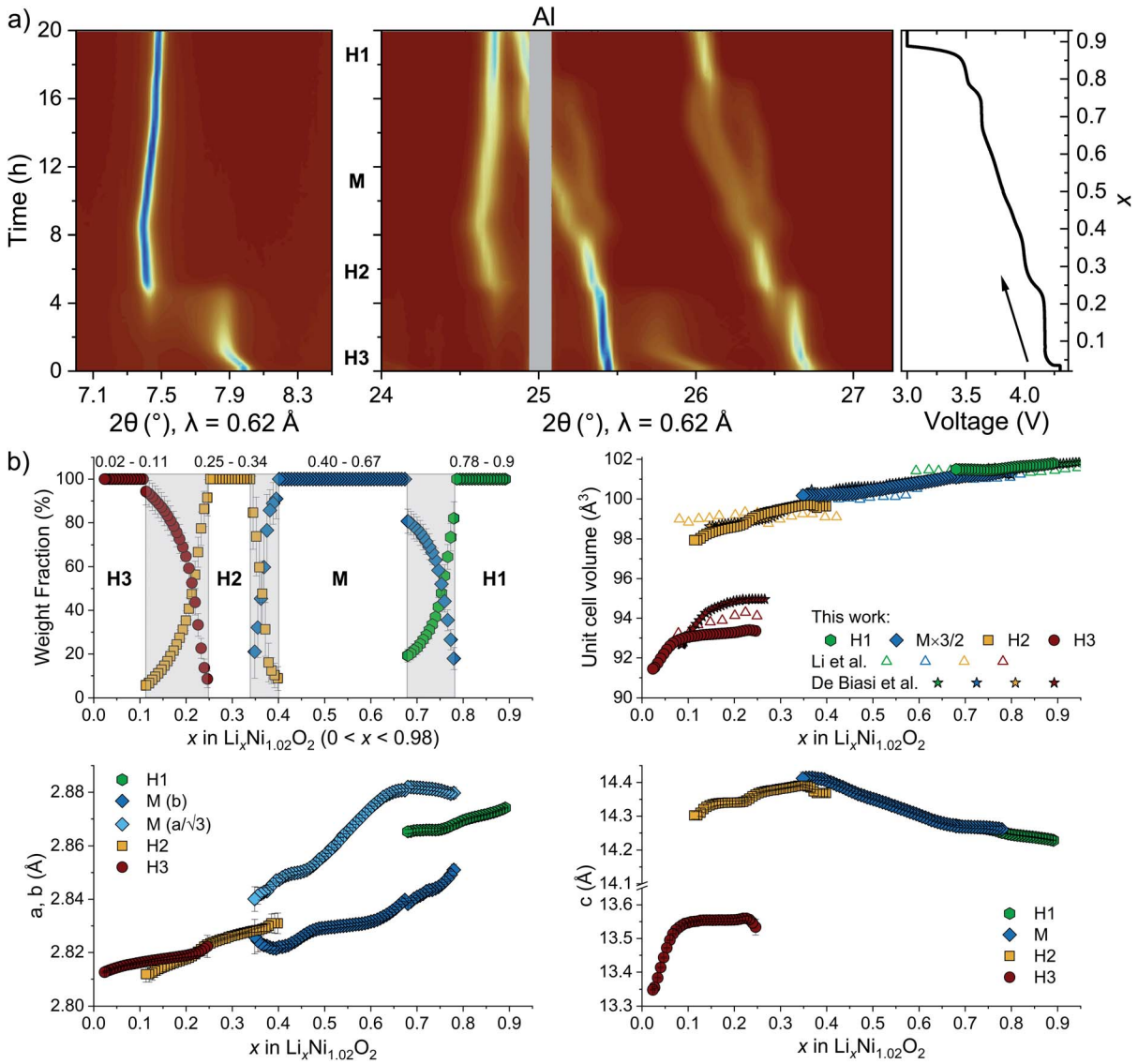

Fig. 3 (a) *Operando* synchrotron XRD patterns recorded during the second discharge of $LiNiO_2$ in pouch cell at C/20 rate. From bottom to top, H3, H2, M and H1 domains can be distinguished. The voltage–composition profile is shown on the right (specific capacity achieved: 239.7 mA h g^{-1}). (b) Unit cell parameters obtained from Rietveld refinement. The unit cell volume data include a comparison with recent experiments in the literature.[7,8] Further structural parameters are gathered in Fig. S6.†

that a long-standing controversy exists about the true nature of the $LiNiO_2$ ground state.[50] We recently found that $LiNiO_2$ is a dynamic Jahn–Teller system with monoclinic symmetry;[50] low intra- and inter-layer correlations prevent the system from experiencing a macroscopic monoclinic shear, and the system appears on average rhombohedral. From a lattice-model point of view, both rhombohedral and monoclinic structures can be mapped to the same lattice, but in the calculation of formation energies, we suggest that the total energy of the $P2_1/c$ cell be used.

For the delithiated compound NiO_2, a structure with O1 stacking ($P\bar{3}m$ s.g.) has been reported at full delithiation,[13,51,52] while under common experimental conditions some residual Li is always present and the experimentally observed H3 phase has O3 stacking ($R\bar{3}m$ s.g.). The calculated energy difference between the O3 and O1 structures is only 10 meV per f.u., within the DFT error, and hence our choice of either O3 or O1 does not affect the shape of the hull. Here, for NiO_2 we choose the reference energy of the rhombohedral O3 structure ($R\bar{3}m$) to better align with the experimental results.

With this choice of boundary phases, we calculated the formation energies of the 499 structures contained in the database. Fig. 4a shows the final DFT and cluster-expanded convex hulls. In Fig. 4b, a prediction error plot shows the correlation between cluster-expanded and target (DFT) mixing energies. For a perfect model, where the predicted value is identical to the target values, all data points would follow the black line. Data points are also color-coded according to the distance of the target energy from the DFT convex hull. Points in dark blue are structures close to the convex hull, which might be relevant stable phases. The Li_xNiO_2 system contains

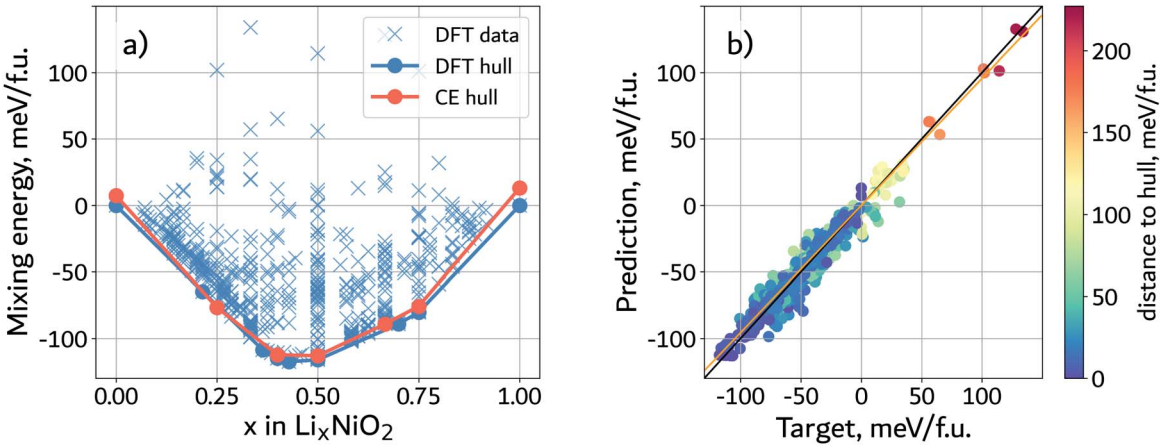

Fig. 4 (a) Calculated formation energies of Li_xNiO_2 together with the calculated (blue) and cluster-expanded (red) convex hulls. (b) Prediction error plot comparing predicted and target DFT mixing energies. The black 45 degree line indicates the perfect fit and is drawn as a guide to the eye, whereas the orange line is the actual fit to our data: $y = 0.9562099x - 0.00222966$. The color map quantifies the energy distance of target energies from the hull.

a surprising amount of nearly-degenerate configurations: 82 structures in our database are within 5 meV per f.u. of the convex hull. The root-mean-square error of the mixing energy over the complete data set is 7.7 meV per f.u.

3.3 Stoichiometric $LiNiO_2$

We calculated the compositional phase diagram of Li_xNiO_2 by performing Monte Carlo simulations in the semi-grand canonical ensemble, as discussed in detail in the Methods section. At 0 K, ordered phases appear at $x = 0.25$ (1/4), 0.4 (2/5), 0.5 (1/2 = 4/8), 0.625 (5/8) and 0.75 (3/4 = 6/8) (described in detail in the next section). This is only partly consistent with previous studies that predicted orderings at 0.25, 0.33, 0.4, 0.5, 0.6, 0.75 and 0.83[14] or 0.125, 0.25, 0.33, 0.5, 0.6, 0.625, 0.67, 0.75, 0.83 and 0.875.[16] A major deviation from the literature is clear at finite temperatures: above 250 K, two miscibility gaps close and a solid solution appears between $x = 1/2$ and 3/4. This feature matches for the first time the wide monoclinic region observed in experiments (Fig. 1). Discrepancies with earlier studies can be ascribed to several concurring factors: the different choice of boundary phases, the availability of a new improved functional, and the realization that geometric frustration requires a careful inspection of ground states.

Phase diagrams also give us access to simulated voltage curves. Voltage profiles contain the same information as compositional phase diagrams because they are related to the derivative of the free energy with respect to Li content, but are more easily compared to experimental data. In Fig. 5b we report the calculated voltage for perfectly stoichiometric $LiNiO_2$ at 300 K compared to the experimental voltage curve for the second discharge already shown in Fig. 3a. One can observe a semi-quantitative match with experiments regarding the position of phase transitions. As expected, the choice of a different ground state for LNO, together with an improved functional, largely corrects LDA's and GGA's voltage underestimation.[53] Arroyo[14] had already observed that allowing for Jahn-Teller distortions would yield lower-energy structures on the convex hull; however, the choice of the PBE functional still resulted in an underestimated voltage profile.

The cluster expansion formalism, however, does not only apply to formation energies, but also to arbitrary scalar properties

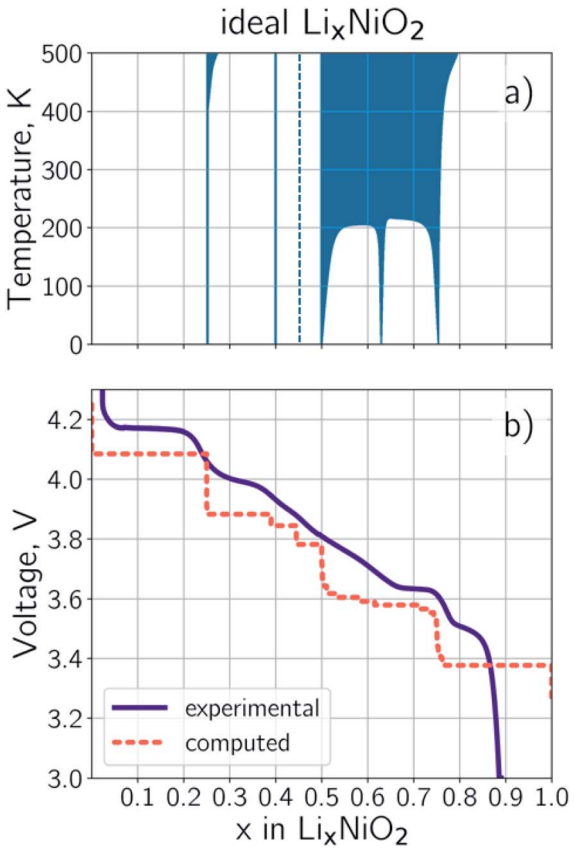

Fig. 5 (a) Calculated phase diagram of perfectly stoichiometric $LiNiO_2$: blue areas indicate one-phase fields; the dashed blue line marks a metastable phase at $x = 0.45$. (b) Comparison between the measured (solid) and calculated (dashed) voltage curve for $LiNiO_2$ at 300 K. Note that the experimental x values are calculated based on the $Li_{0.98}Ni_{1.02}O_2$ stoichiometry.

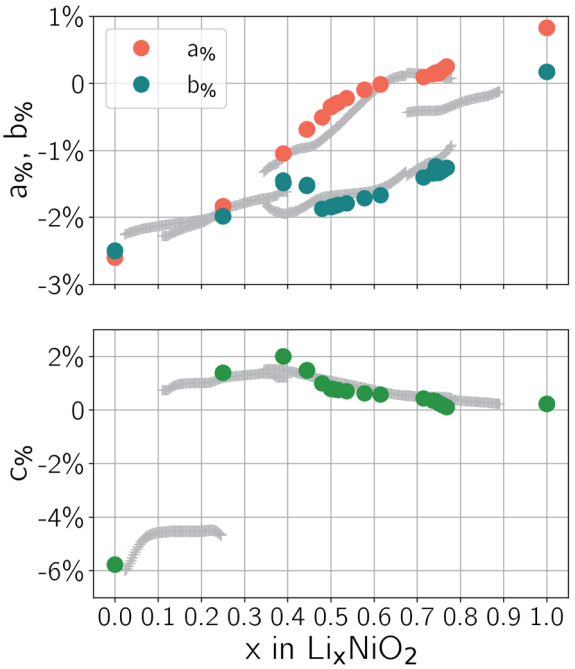

Fig. 6 Percentual variations of cluster-expanded lattice constants of Li_xNiO_2 as a function of lithium content at 300 K. Experimental values from Fig. 3b are overlayed as light grey crosses. Note that the experimental x values are calculated based on the $Li_{0.98}Ni_{1.02}O_2$ stoichiometry.

that depend on the atomic arrangement. Using the same dataset, we trained a cluster expansion to predict the lattice constants of Li_xNiO_2 structures. Fig. 6 shows the predicted percentual changes of the lattice constants as a function of lithium content. As with the phase diagram, we notice gaps corresponding to two-phase fields as a result of operating in the semi-grand canonical ensemble; therefore we can only discuss trends for one-phase regions. For a straightforward comparison to experiments, we also plot the relative variations of the lattice parameters already shown in Fig. 3b. Starting with low Li content, the two basal lattice constants a and b are identical up to about $x = 0.4$, thus indicating a hexagonal symmetry as identified by XRD. At $0.4 < x < 0.75$, the basal lattice constants split, as befits a monoclinic distortion, again in good agreement with the experiment. At $x > 0.75$, the hexagonal phase H1 should emerge, again with $a = b$. However, our reference for fully lithiated $LiNiO_2$ is the monoclinic $P2_1/c$, as previously discussed.[50] At high Li content, given the still large amount of Ni^{3+}, it is likely that the dynamic behavior of the Jahn-Teller distortions may survive, giving H1 the familiar apparent rhombohedral symmetry. However, a cluster expansion based on a static model cannot account for the dynamic behavior, and therefore our cluster-expanded lattice parameters end with $a \neq b$ at $x = 1$. The behavior of the axial lattice constant, c, is relatively more straightforward and follows closely the experimental trend, including a maximum at about $x = 0.4$. The computed absolute values (Fig. S7†) are slightly lower than the experimental results in Fig. 3, which is no surprise as the cluster expansion is trained on 0 K DFT values.

3.3.1 Notable Li orderings

A commonly employed tool used to better visualize phase transitions occurring in cathode materials from the capacity-voltage (or composition-voltage) curve is the plot of the inverse derivative dq/dV (or $d|x|/dV$) against the voltage. In such a plot, intense peaks appear at voltage plateaus in the x–V curve, clearly marking first order transitions. Minima between different peaks identify stable single-phase compositions. An example of such a curve is provided in Fig. 7, which refers to the experimental curve of Fig. 3a and 5. One can immediately notice that the three most intense peaks at 3.66 V, 3.88 V and 4.17 V correspond to the phase transitions observed by XRD, namely H1 → M, M → H2 and H2 → H3.

These are also reproduced by our computed voltage curve in Fig. 5, with an offset of about 0.1–0.2 V. However, some discrepancies remain since Fig. 5 reports a computed curve for perfect LNO, which does not reflect a real sample with off-stoichiometry defects. We will show in the following how this can be improved (Fig. 9). Here, it is important to note the fine structure of the $d|x|/dV$ curve in Fig. 7. In addition to the aforementioned main peaks, others are present that do not correspond to any phase transition macroscopically observed by XRD. Nonetheless, the position of the minima can be tracked and used to identify the voltage and composition of metastable phases, which may possibly be stabilized at the local scale.

In LNO, the $d|x|/dV$ minima can be experimentally observed at compositions of $x = 3/4$, $5/8$, $1/2$, $2/5$ and $1/4$. We find that these are exactly the 0 K stable phases predicted by our computational results of Fig. 5. These compositions are stabilized by peculiar Li-vacancy ordering, depicted in Fig. 8 and S8.† As suggested by Arroyo,[14,15,55] these ordered structures may be further stabilized by the cooperative charge ordering of JT-active Ni^{3+} cations and non-JT-active Ni^{4+} ones. The orderings we find

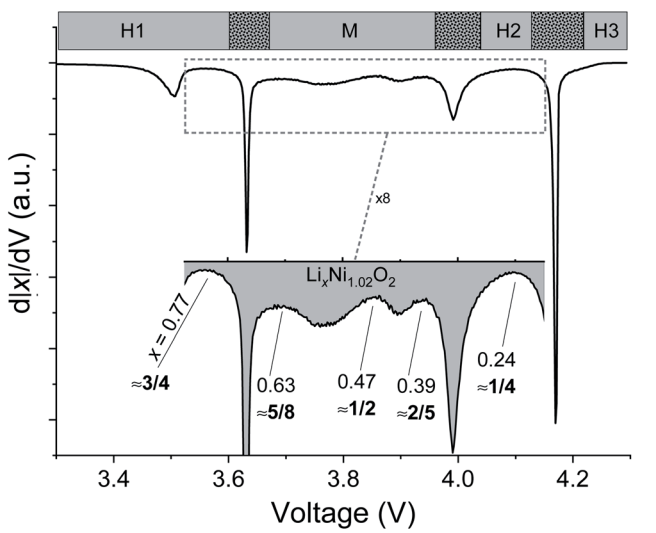

Fig. 7 Experimental $d|x|/dV$ curve for $Li_xNi_{1.02}O_2$. The zoomed-in region (grey area) highlights the features of the $d|x|/dV$ curve in the monoclinic region, where minima of the curve correspond to special values of x, matching those found to stabilize specific orderings at 0 K in our phase diagram of Fig. 5.

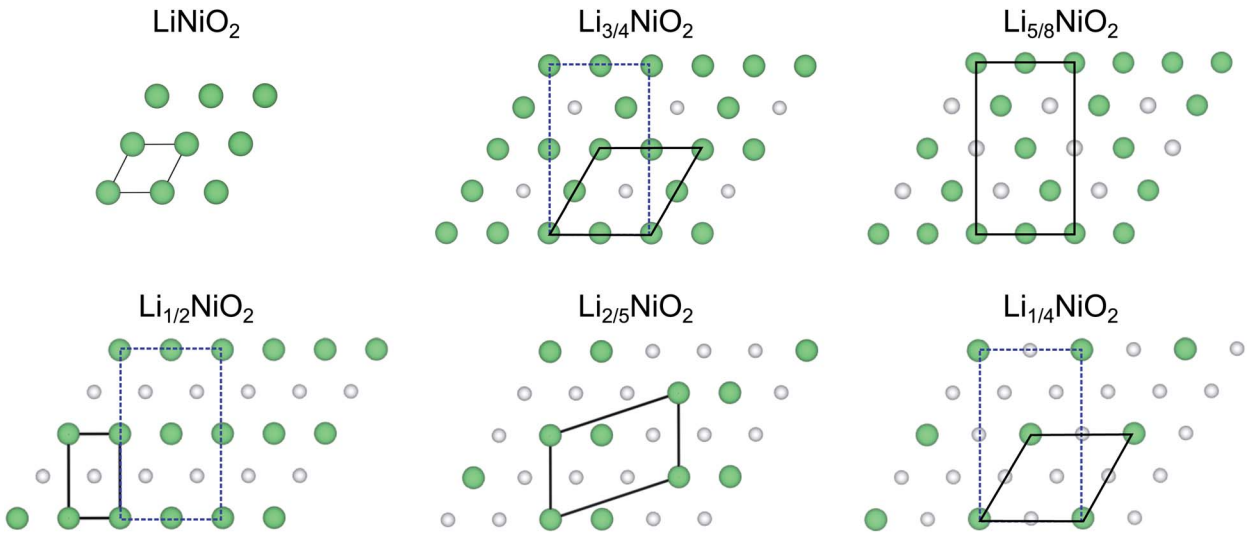

Fig. 8 Li-vacancy orderings in the Li sublattice at 0 K. Li ions and vacancies are depicted as green and white spheres, respectively. Basal unit cells are outlined with solid black lines and match those reported by Peres *et al.*;[49,54] the one reported in dashed blue is a notable supercell discussed in the main text. Note that all compositions have hexagonal or monoclinic structures with O3 stacking, with the exception of $Li_{5/8}NiO_2$ which is a O6 structure.

also agree with experimental literature reports. $x = 1/2$ is well-established,[49,54,56] featuring alternating rows of full and vacant Li sites, and can be indexed in the monoclinic $P2/m$ space group. Peres *et al.*[49,54] showed that $x = 3/4$ corresponds to a similar ordering, where the empty row has now alternating vacant and filled Li sites. A unit cell twice as large is then needed to describe it (Fig. 8). In both cases, these orderings correspond to those we find computationally. Peres also argued that the $x = 1/2$ and $x = 3/4$ orderings drive the formation of the monoclinic region; although we agree, we suggest an extended interpretation. We find a stable structure at $x = 5/8$, and note the interesting sequence $4/8 - 5/8 - 6/8$. The corresponding Li-vacancy ordering is different depending on the viewing direction. It can be either considered as one filled Li row alternated with another row containing one out of three occupied Li sites, or as a filled row alternated by three half-filled rows. Either way, the unit cell needs to be further enlarged to describe such an ordering. Firstly, by doubling again the basal cell surface. More importantly, $x = 5/8$ is the only Li-vacancy ordering that is not described in a single Li layer, but that actually requires doubling along the axial direction. Hence $x = 5/8$ can be described as a O6 structure. This perfectly matches the electron diffraction data of Peres *et al.*,[49,54] who studied $Li_{0.63}NiO_2$ and reported for that composition a $C2/m$ unit cell with doubled unit cell parameters $a = 10.138$ Å, $b = 5.656$ Å, and $c = 8.223$ Å ($\beta = 145.17°$) with respect to the monoclinic one observed by XRD. We attribute this for the first time to the actual composition $x = 5/8$. Although the choice of DFT supercells may in some cases influence the stability of different orderings, the excellent match to past reports and the fact that the $d|x|/dV$ curve exhibits a clear minimum at $x = 0.63 = 5/8$ is a strong argument supporting the true existence of this ordering. Finally, the stable structures we find at $x = 2/5$ and $x = 1/4$ have never been observed experimentally to yield any particular superstructure (with one exception for $x = 1/4$ (ref. 54)); however they occurred in all previous computational studies, and they clearly show up as minima in the $d|x|/dV$ curve, again supporting their existence. Moreover, by refinement of the *operando* XRD data we showed how $x = 2/5$ marks the end of the monoclinic region whereas $x = 1/4$ marks the end of the H2 phase region.

Despite a good match between calculated and experimental electrochemical and structural properties, the voltage profile for stoichiometric LNO is still a step function: a truly realistic LNO model should account for deviations from perfect stoichiometry, both in the form of native Ni excess (Ni_{Li}) and artificially introduced Ni substituents. The main obstacle to train a cluster expansion for such systems lies in the computational effort needed to describe adequately small defect concentrations. In the following, we present a surrogate model that accounts—at least qualitatively—for such effects without the need to reparameterize the cluster expansion.

3.4 Deviations from stoichiometric $LiNiO_2$

Local disorder disrupts Li ordering by pinning Li ions (in the case of "Li-anchoring" substituents) or vacancies in the Li sublattice (in the case of Ni_{Li}). We modelled local disorder due to off-stoichiometry and Ni substitution imposing constraints on the site occupancies of our lattice model.

3.4.1 Off-stoichiometry. To model off-stoichiometry, we make use of the approximation that, after the first charge, every Ni_{Li} prevents seven Li sites per Ni_{Li} from being re-occupied.[20] The seven sites are arranged in a hexagonal cluster: the center of the hexagon corresponds to Ni_{Li} and the vertexes are the six Li nearest-neighbors (Fig. 2a). In our lattice model, we populated those sites with vacancies and deactivated their ability to host Li. In the computed phase diagram (Fig. 9a), the solid solution at $x = 0.37–0.73$ is now separated from another single-phase region at x

= 0.77–0.86 by a narrow phase transition and bears a striking resemblance to the experimental phase diagram in the H1 and M regions (*cf.* the entries labelled "This work" in Fig. 1).

The computed voltage curve for $Li_xNi_{1.02}O_2$ (Fig. 9b) is distinctly smoother than its stoichiometric counterpart especially in the intermediate Li content region. The lost capacity is clearly due to the unavailable Li sites and is a good fit to the experimental curve. At high state of charge, the distinct H2/H3 plateau is still visible but is smaller compared to stoichiometric Li_xNiO_2, as it extends only to $x = 0.215$ rather than 0.25. The presence of pinned vacancies partly disrupts what was the $Li_{0.25}NiO_2$ ordering in stoichiometric LNO: while the system still tries to install the characteristic sequence of alternating empty and half-filled rows, some Li positions are now occupied by pinned vacancies (Fig. S9†), effectively lowering the overall Li concentration. This effect intensifies with increasing Ni_{Li} concentration: at 7% Ni_{Li} the former "$Li_{0.25}NiO_2$" phase shows a Li concentration of only 12%. This behavior hence indicates that for increasing Ni_{Li} concentration the miscibility gap between H2 and H3 narrows, thereby eventually eliminating the H2–H3 phase transition, as expected experimentally.

On the other hand, while the H2–H3 two-phase region we observe behaves as expected, the H2 and H3 single-phase domains are too narrow. At 300 K, H2 is still much narrower than the experimentally reported H2 phase (Fig. 1) and its domain only widens at higher temperatures. This behavior might be ascribed to effects neglected by our model. Since Ni_{Li} is described only in the form of pinned vacancies, without explicitly accounting for physical Ni ions on Li sites, we might underestimate the influence of vibrational entropy especially at low Li concentrations, when extra Ni occupy a significant portion of the populated Li sublattice sites.

While analogous considerations are valid for all phases in our study, including H3, we will demonstrate in the following that stacking faults are also an important reason of discrepancy at low Li content.

3.4.2 Ni substitution. Li ordering and diffusion are also affected by substitutional elements (dopants). When Li migration is hindered, changes in the phase diagram and voltage profile can be seen at high states of charge.[27] A substituent like Al, for example, prevents an equivalent amount of Li from leaving the structure[27] (Fig. 2b) due to its redox-inactivity. In general, substituents are also likely to impact the amount of Ni_{Li} in the structure, and therefore multiple effects overlap. In this respect, Al is "well behaved", in that the percentage of Ni_{Li} only slightly changes with the extent of Ni substitution (at low Al content). In our lattice model, under the assumption that the substituent does not affect the amount of extra Ni in the Li lattice, we imposed full occupancy of a certain amount of Li sites and forbade them to host Li vacancies.

Fig. 10 illustrates how voltage profiles change as a function of substituent content (0–10%) in the presence of 3% Ni_{Li}. Additionally, the inset compares the computed and experimental voltage curves for LNO containing 5% Al and 3% Ni_{Li}

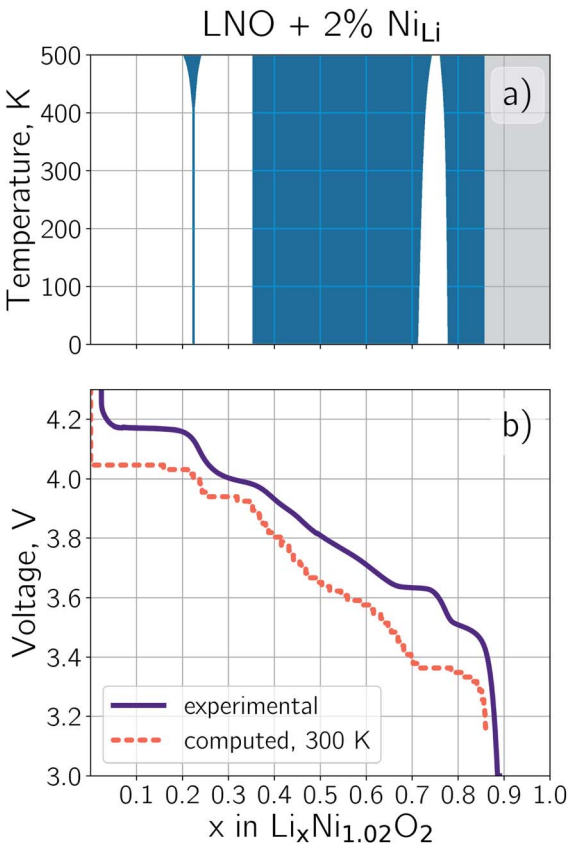

Fig. 9 Calculated phase diagram of $Li_xNi_{1.02}O_2$ (a): blue areas indicate one-phase fields, the grey area is inaccessible due to the pinned vacancies in the lattice. (b) Comparison between the measured (solid) and calculated (dashed) voltage curve for $Li_xNi_{1.02}O_2$ at 300 K.

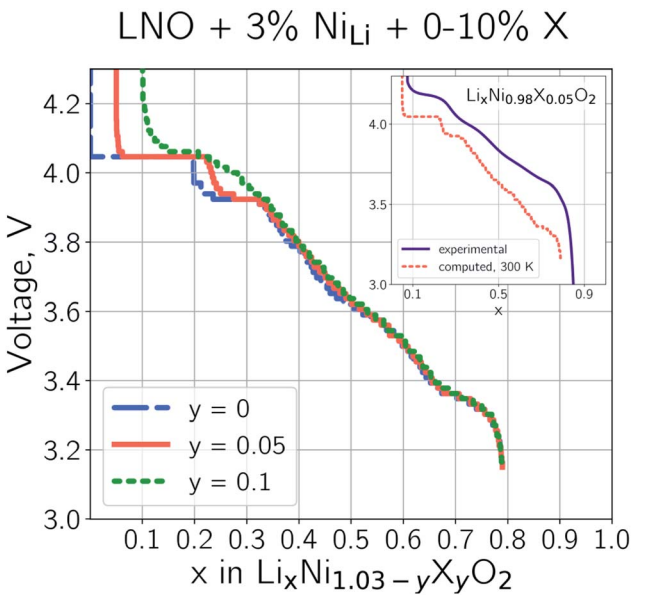

Fig. 10 Evolution of computed voltage profiles as a function of substituent content and in the presence of 3% Ni_{Li} at 300 K. The inset shows the comparison between the experimental voltage curve for $Li_xNi_{0.98}Al_{0.05}O_2$ (solid) and the calculated voltage curve for $Li_xNi_{0.98}X_{0.05}O_2$ at 300 K (dashed), where "X" is a Ni substituent that anchors an equivalent amount of Li ions, such as Al.

(Table S2†). With a 5% doping, the two-phase H2/H3 plateau is narrower, although not eliminated. With 10%, the voltage profile is distinctly smoother: the H2/H3 phase transition is sensibly reduced and the M/H2 transition is suppressed. This fits well with experimental results.[27,57] It also supports the fact that cobalt does not yield the same mitigating effects on phase transitions as other dopants:[27] Co is too similar to Ni (isovalent, redox active) to effectively disrupt Li/vacancy orderings.

3.5 Direct *operando* observation of stacking faults and strain during the H2–H3 phase transition

Our computational results show excellent agreement with experimental ones at intermediate Li contents, *i.e.* roughly for $0.3 < x < 0.8$. However, the agreement worsens at low Li content and, to a lower extent, at high Li content. The source of such discrepancy at high Li content is known from literature and is due to slow kinetics of Li ions at such high concentrations.[6] This can be related to: (i) the lack of di-vacancies allowing for fast Li diffusion, (ii) the small value of the Li interlayer spacing at these Li concentrations, and (iii) the presence of Ni_{Li} defects.[21,24] Experimentally, it has been shown that a kinetic plateau exists at 3.5 V in the composition–voltage curve under slow cycling conditions such as C/20 (in fact, it can also be seen in the experimental curve in Fig. 9), while such plateau and the relative capacity are lost at higher rates.[8] We further prove this here by showing that even small temperature differences can have a drastic effect on this kinetic plateau (Fig. S10†): cycling LNO at 45 °C instead of 25 °C results in significant additional capacity, mostly located at 3.5 V. Obviously, such a kinetic behavior is not captured within a static lattice model.

Understanding the source of discrepancy in the delithiated domain of LNO, *i.e.*, when the H2–H3 transition occurs, is more complex. Going back to the *operando* XRD data discussed previously, we can find further evidence of a peculiar behavior in the goodness of fit of the Rietveld refinement (R_{Bragg}, see Fig. S6 in the ESI†). While the hexagonal models of H1 and H2 and the monoclinic one of the M phase allow to properly reproduce the diffraction data, the Rietveld fit quality drastically worsens in the H2–H3 biphasic region. Initially, it also remains poor in the single-phase H3 region, but it improves with further delithiation. Such a behavior clearly indicates that structural phenomena beyond those considered so far must be taken into account during the H2–H3 phase transition.

Fig. 11a shows a selected angular domain during the biphasic H2–H3 region and during the single-phase H3 one. Two facts can immediately be recognized. First, the 110 and 113

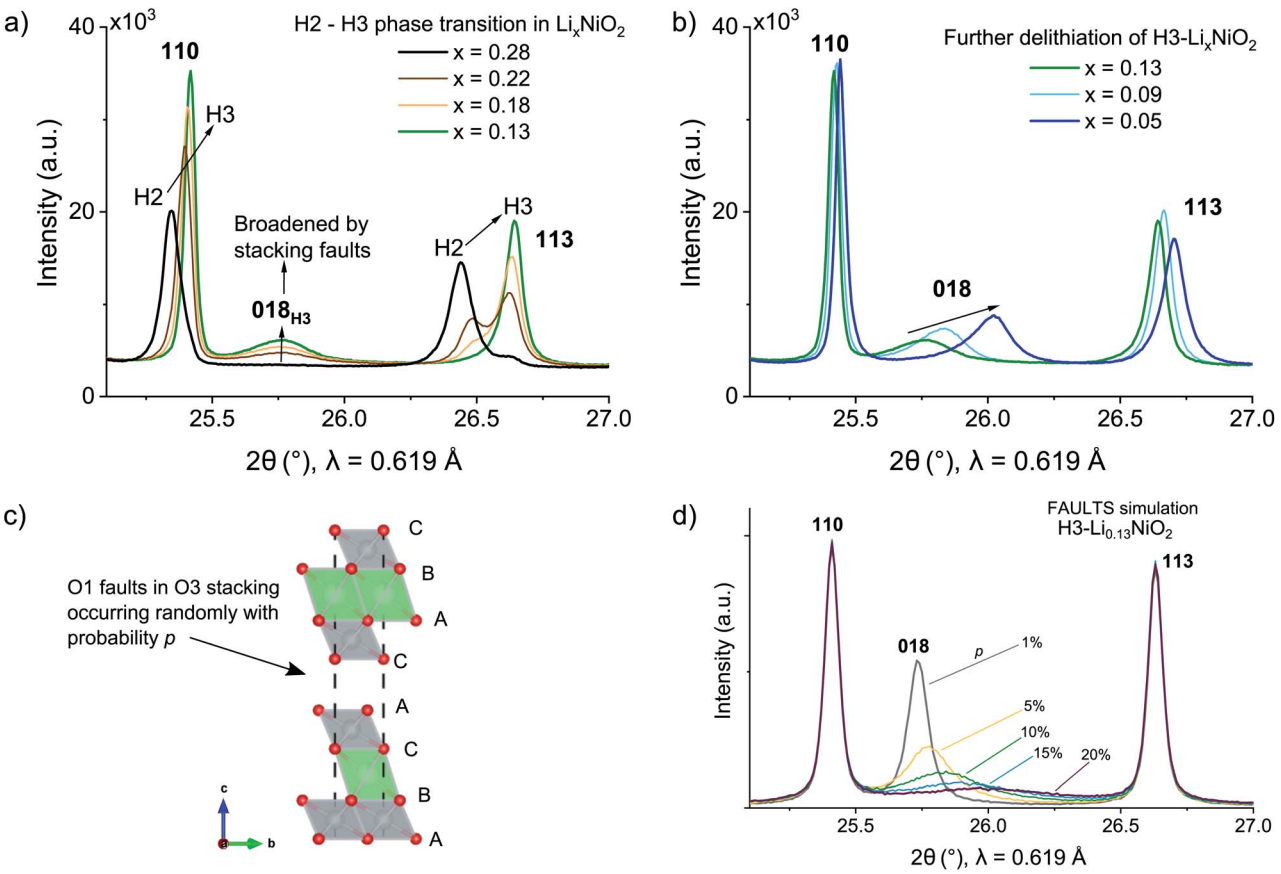

Fig. 11 *Operando* synchrotron XRD patterns obtained during the H2–H3 phase transition (a) and during the H3 phase evolution (b). The patterns highlight the broad 018_{H3} reflection. (c) Atomic model of the stacking faults, occurring as completely empty layers with O1 stacking. (d) Simulation of the XRD patterns carried out with FAULTS at different probabilities *p* of random O1 stacking faults into the H3 structure (O3 stacking).

peaks have different widths in both phases. This is indicative of the existence of anisotropic strain broadening that develops during the H2–H3 transition due to the large volume difference between the two phases. Thus, significant elastic energy contributions may be expected. Secondly, the 018 peak of the H3 phase is unusually weak and broad. This behavior can be explained in line with the results of Croguennec *et al.*[52] These authors reported the existence of stacking faults in *ex situ* samples of delithiated LNO, in particular of O1-type empty layers within the O3-type predominant stacking. To verify that indeed such specific stacking faults can explain the broadening of the 018 peak, we conducted a simulation using the FAULTS program.[48] Fig. 11c gathers the main result: random O1-type faults affect the 018 reflection dramatically, while leaving the neighboring ones unaffected. Our simulation also allows us to estimate the degree of faulting: a stacking fault probability between 10 and 15% reproduces the experimentally observed broadening at the beginning of the H2–H3 transition. Interestingly, as the H3 phase further delithiates, the 018 peak gains intensity and narrows, indicating a lower density of faults of about 5% toward composition $Li_{0.02}NiO_2$, in line with the improved fitting results. One should note the difference between $LiNiO_2$ and $LiCoO_2$: in LNO we find random O1 faults, while in $LiCoO_2$ O1 and O3 layers have been observed to order along the *c* axis, resulting in a staged phase called H1–3.[41,58] The staging phase transition in LCO is possible thanks to the absence of Co in the Li layer. In LNO, Ni_{Li} likely hinders the layers gliding, causing faulting instead. In fact, the development of stacking faults also helps explain the differences in the H2–H3 phase transition between different authors. These defects strongly depend on the exact crystal structure, composition and morphology of the material. Hence even minor variations in, *e.g.*, the amount of Ni_{Li}, or the homogeneity of doping, can strongly influence the amount and evolution of stacking faults, ultimately leading to poorly reproducible results among nominally identical samples.

4 Discussion and conclusions

Despite the fact that the (de)intercalation pathway and the phase diagram of LNO have been experimentally studied for almost three decades and despite the constant improvement of *in situ*/*operando* setups, the results have often showed unsatisfactory reproducibility, especially in the highly delithiated

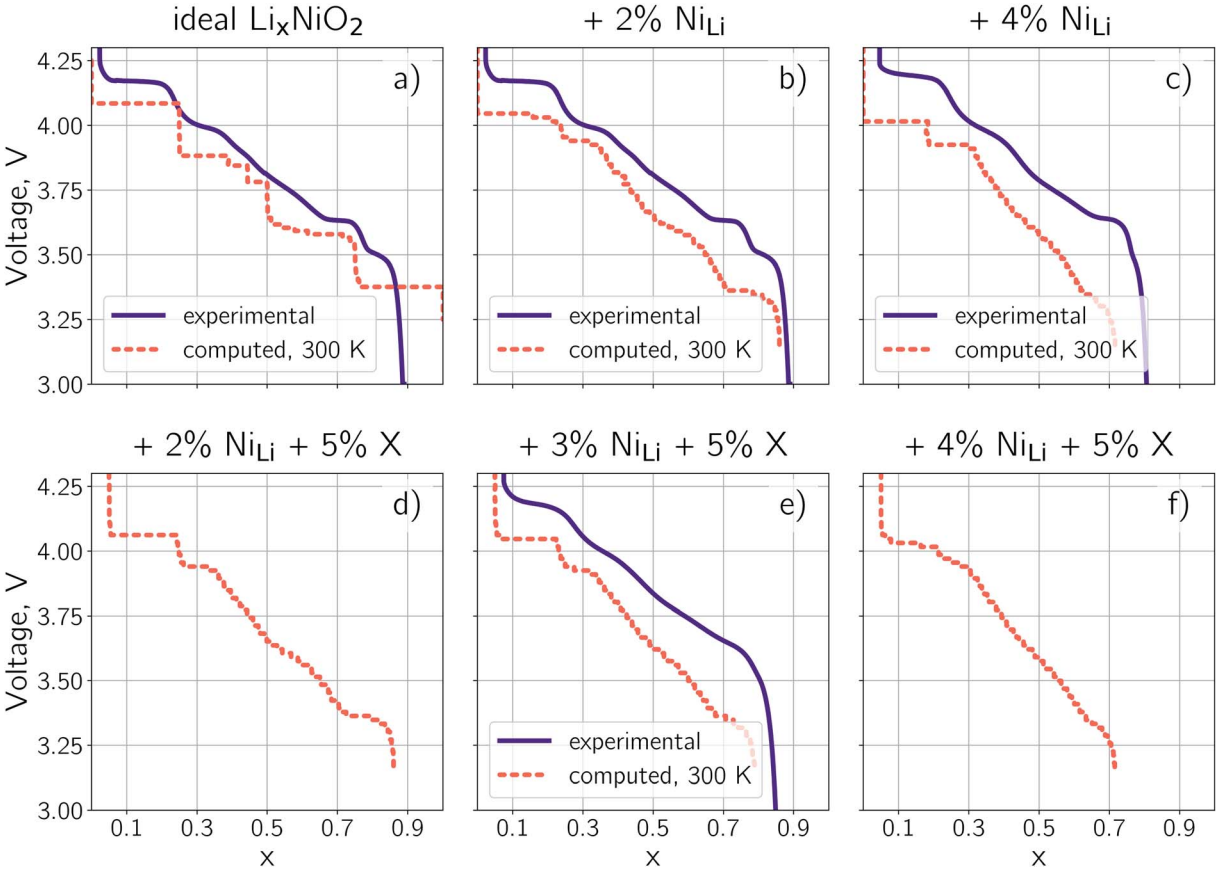

Fig. 12 Evolution of voltage profiles as a function of structural complexity: stoichiometric LNO (a); off-stoichiometric LNO with 2% Ni_{Li} compared to the experimental voltage curve for $Li_xNi_{1.02}O_2$ (b); off-stoichiometric LNO with 4% Ni_{Li} compared to the respective experimental voltage curve (Table S3†) (c); off-stoichiometric LNO with 2% Ni_{Li} and 5% Ni substituent "X" (d); off-stoichiometric LNO with 3% Ni_{Li} and 5% Ni substituent "X" compared to the experimental voltage curve for $Li_xNi_{0.98}Al_{0.05}O_2$ (e); off-stoichiometric LNO with 4% Ni_{Li} and 5% Ni substituent "X" (f).

domain. This points toward a deeper, material-related cause of discrepancy, as we have ascertained with our synchrotron XRD data. Experimentally, we showed with synchrotron XRD data that when LNO is delithiated beyond the H2 phase, stacking faults dominate its behavior. Such defects are heavily sample-dependent and can be influenced by a myriad of factors, the most important being the amount of Ni_{Li} defects. This determines the large scattering of experimental results.

From a computational point of view, an unrealistic staircase-like computed voltage curve is an unavoidable feature of perfectly stoichiometric LNO, regardless of the choice of the functional and boundary phases: a fair comparison with experiments can only be made by addressing deviations from the ideal stoichiometry. By imposing predetermined occupancies of the Li sublattice, we have created an effective surrogate model that accounts for the presence of excess Ni. A distinct smoothing of the computed voltage curves ensues, accompanied by an unprecedented match to the experimental voltage profile (Fig. 9) and phase diagram (Fig. 1). An H1 domain extends from full lithiation (or from 0.9 after the first charge) to 0.78. Then, a monoclinic domain is found, whose nature is clarified as a sequence of 0 K Li-vacancy orderings at $x = 3/4$, 5/8, 1/2 and 2/5. Their signature remains in the $d|x|/dV$ curve but they are macroscopically destabilized by temperature and by Ni_{Li} defects, resulting in the familiar broad monoclinic domain observed by XRD that for the first time is also present in the computed phase diagram and voltage profile. The H2 and H3 domains are also observed, as is the H2–H3 two-phase region and its behavior as a function of defect concentration: the H2 → H3 plateau shrinks linearly as a function of defect concentration, ranging from 0.25 for perfectly stoichiometric $LiNiO_2$ to 0.1225 at $N_{NiLi} = 7\%$. However, the H2 and H3 single phase domains do not fully match the experimental ones, mostly because the computations cannot account for the stacking faults developing in the structure.

Our model can be extended to include (the effect of) some substitutional elements, which are shown to narrow the M → H2 and H2 → H3 phase transitions. Despite its simplicity, this surrogate model is relatively flexible, in that it allows to superimpose independent contributions and simulate different scenarios, depending on the amount of blocked or fixed Li sites. An example is shown in Fig. 12, where different voltage curves are calculated as function of varying structural complexity, showing the progressive disappearance of phase transitions for different substituent concentrations.

Overall, our model does satisfactorily reproduce the phase diagram and voltage curve of a "real" LNO sample, *i.e.* one that contains small amounts of Ni_{Li} defects and substitutional elements. Hence these results significantly advance the understanding of LNO and its phase diagram: the model provides an unprecedented match between simulations and experiments, being particularly effective at reproducing the monoclinic domain and drawing a correspondence between electrochemical features and Li-vacancy orderings.

Nevertheless, we need to address the limitations of this approach. Stacking faults at low Li content and sluggish kinetics at high Li content cannot be accounted for within a lattice model. The same applies to the experimental inability to fully delithiate samples with increasing off-stoichiometry (*cf.* Fig. 12b and c). Furthermore, being "agnostic" to the chemical nature of the foreign species, the model does not reproduce variations in the average voltage. Finally, the effect of higher defect concentrations on phase stability is not taken into account.

Although an ad-hoc study is needed to fully grasp the exact behavior of any given substituent, our model makes a strong argument that the major effect of substitutional strategies in limited concentration is the simple disruption of Li orderings, which in turn results in the establishment of solid solutions and the progressive elimination of phase transitions. A sort of Pareto principle, where 20% of the causes (order disruption) results in 80% of the consequences (quantitative smoothing of voltage profiles). This behavior is common to all industrially relevant Ni-rich cathode active materials that are derived, but do not excessively diverge, from LNO. Likewise, a similar approach could be used for homeotypic cathodes such as LCO. In general, provided that a given CAM can be mapped onto a lattice model, our approach can be applied to investigate the macroscopic effects of relatively small defect concentrations. This is valuable as real experimental materials are likely to contain defects, either because thermodynamically hard to avoid (*e.g.*, Ni_{Li} in LNO or antisite defects in $LiFePO_4$) or present by design, as is the case for the small amounts of substituents (often ≈ 1%) present in commercial cathode materials. Our model can thus be extended in the future to predict the behavior of such compounds as well without the need to parameterize a cluster expansion on exceedingly large supercells.

Conflicts of interest

There are no conflicts to declare.

Acknowledgements

This work was supported by BASF SE. The authors acknowledge MSPD and the ALBA synchrotron for the beamtime awarded under proposal 2018093051.

References

1 G. E. Blomgren, *J. Electrochem. Soc.*, 2017, **164**, A5019–A5025.
2 Project by BMW, BASF, *Samsung SDI and Samsung Electronics to enhance sustainable cobalt mining*, https://www.basf.com/global/en/who-we-are/sustainability/responsible-partnering/cobalt-initiative.html.
3 E. A. Olivetti, G. Ceder, G. G. Gaustad and X. Fu, *Joule*, 2017, **1**, 229–243.
4 J. R. Dahn, U. Vonsacken and C. A. Michal, *Solid State Ionics*, 1990, **44**, 87–97.
5 T. Ohzuku, A. Ueda and M. Nagayama, *J. Electrochem. Soc.*, 1993, **140**, 1862–1870.
6 M. Bianchini, M. Roca-Ayats, P. Hartmann, T. Brezesinski and J. Janek, *Angew. Chem., Int. Ed.*, 2019, **58**, 2–27.

7 L. de Biasi, A. Schiele, M. Roca-Ayats, G. Garcia, T. Brezesinski, P. Hartmann and J. Janek, *ChemSusChem*, 2019, **12**, 2240–2250.
8 H. Li, N. Zhang, J. Li and J. R. Dahn, *J. Electrochem. Soc.*, 2018, **165**, A2985–A2993.
9 C. Delmas, M. Ménétrier, L. Croguennec, S. Levasseur, J. Pérès, C. Pouillerie, G. Prado, L. Fournès and F. Weill, *Int. J. Inorg. Mater.*, 1999, **1**, 11–19.
10 W. Li, J. Reimers and J. Dahn, *Solid State Ionics*, 1993, **67**, 123–130.
11 H. Arai, S. Okada, H. Ohtsuka, M. Ichimura and J. Yamaki, *Solid State Ionics*, 1995, **80**, 261–269.
12 C. Delmas, C. Fouassier and P. Hagenmuller, *Phys. B*, 1980, **99**, 81–85.
13 L. Croguennec, C. Pouillerie and C. Delmas, *Solid State Ionics*, 2000, **135**, 259–266.
14 M. E. Arroyo y de Dompablo, A. Van der Ven and G. Ceder, *Phys. Rev. B*, 2002, **66**, 064112.
15 M. E. Arroyo y de Dompablo and G. Ceder, *J. Power Sources*, 2003, **119–121**, 654–657.
16 H. Das, A. Urban, W. Huang and G. Ceder, *Chem. Mater.*, 2017, **29**, 7840–7851.
17 C. S. Yoon, D.-W. Jun, S.-T. Myung and Y.-K. Sun, *ACS Energy Lett.*, 2017, **2**, 1150–1155.
18 F. Kong, C. Liang, L. Wang, Y. Zheng, S. Perananthan, R. C. Longo, J. P. Ferraris, M. Kim and K. Cho, *Adv. Energy Mater.*, 2019, **9**, 1802586.
19 A. Rougier, P. Gravereau and C. Delmas, *J. Electrochem. Soc.*, 1996, **143**, 1168–1175.
20 C. Delmas, J. Pérès, A. Rougier, A. Demourgues, F. Weill, A. Chadwick, M. Broussely, F. Perton, P. Biensan and P. Willmann, *J. Power Sources*, 1997, **68**, 120–125.
21 K. Kang and G. Ceder, *Phys. Rev. B*, 2006, **74**, 094105.
22 F. Kong, C. Liang, R. C. Longo, Y. Zheng and K. Cho, *J. Power Sources*, 2018, **378**, 750–758.
23 S.-T. Myung, F. Maglia, K.-J. Park, C. S. Yoon, P. Lamp, S.-J. Kim and Y.-K. Sun, *ACS Energy Lett.*, 2017, **2**, 196–223.
24 M. D. Radin, S. Hy, M. Sina, C. Fang, H. Liu, J. Vinckeviciute, M. Zhang, M. S. Whittingham, Y. S. Meng and A. Van der Ven, *Adv. Energy Mater.*, 2017, **7**, 1602888.
25 W. Li, B. Song and A. Manthiram, *Chem. Soc. Rev.*, 2017, **46**, 3006–3059.
26 L. de Biasi, A. O. Kondrakov, H. Geßwein, T. Brezesinski, P. Hartmann and J. Janek, *J. Phys. Chem. C*, 2017, **121**, 26163–26171.
27 H. Li, M. Cormier, N. Zhang, J. Inglis, J. Li and J. R. Dahn, *J. Electrochem. Soc.*, 2019, **166**, A429–A439.
28 G. Ceder, Y. M. Chiang, D. R. Sadoway, M. K. Aydinol, Y. I. Jang and B. Huang, *Nature*, 1998, **392**, 694–696.
29 C. Pouillerie, L. Croguennec, P. Biensan, P. Willmann and C. Delmas, *J. Electrochem. Soc.* , 2000, **147**, 2061.
30 G. Kresse and J. Hafner, *Phys. Rev. B: Condens. Matter Mater. Phys.*, 1993, **47**, 558–561.
31 G. Kresse and J. Hafner, *Phys. Rev. B: Condens. Matter Mater. Phys.*, 1994, **49**, 14251–14269.
32 G. Kresse and J. Furthmüller, *Comput. Mater. Sci.*, 1996, **6**, 15–50.
33 G. Kresse and J. Furthmüller, *Phys. Rev. B: Condens. Matter Mater. Phys.*, 1996, **54**, 11169–11186.
34 P. E. Blochl, *Phys. Rev. B: Condens. Matter Mater. Phys.*, 1994, **50**, 17953–17979.
35 G. Kresse and D. Joubert, *Phys. Rev. B: Condens. Matter Mater. Phys.*, 1999, **59**, 1758–1775.
36 H. Peng, Z.-H. Yang, J. P. Perdew and J. Sun, *Phys. Rev. X*, 2016, **6**, 041005.
37 A. Chakraborty, M. Dixit, D. Aurbach and D. T. Major, *npj Comput. Mater.*, 2018, **4**, 60.
38 J. M. Sanchez, F. Ducastelle and D. Gratias, *Phys. A*, 1984, **128**, 334–350.
39 D. De Fontaine, *Solid State Phys.*, 1994, **47**, 33–176.
40 A. Van der Ven, M. K. Aydinol, G. Ceder, G. Kresse and J. Hafner, *Phys. Rev. B: Condens. Matter Mater. Phys.*, 1998, **58**, 2975–2987.
41 A. Van der Ven, M. K. Aydinol and G. Ceder, *J. Electrochem. Soc.*, 1998, **145**, 2149–2155.
42 A. Van der Ven and G. Ceder, *Electrochem. Commun.*, 2004, **6**, 1045–1050.
43 A. van de Walle and G. Ceder, *Rev. Mod. Phys.*, 2002, **74**, 11–45.
44 M. Ångqvist, W. A. Muñoz, J. M. Rahm, E. Fransson, C. Durniak, P. Rozyczko, T. H. Rod and P. Erhart, *Adv. Theory Simul.*, 2019, **2**, 1900015.
45 A. van de Walle and M. Asta, *Modell. Simul. Mater. Sci. Eng.*, 2002, **10**, 521–538.
46 F. Fauth, I. Peral, C. Popescu and M. Knapp, *Powder Diffr.*, 2013, **28**, S360–S370.
47 J. Rodriguez-Carvajal, *Phys. B*, 1993, **192**, 55–69.
48 M. Casas-Cabanas, M. Reynaud, J. Rikarte, P. Horbach and J. Rodriguez-Carvajal, *J. Appl. Crystallogr.*, 2016, **49**, 2259–2269.
49 J. P. Peres, F. Weill and C. Delmas, *Solid State Ionics*, 1999, **116**, 19–27.
50 S. Sicolo, M. Mock, M. Bianchini and K. Albe, *Chem. Mater.*, 2020, **32**, 10096–10103.
51 L. Seguin, G. Amatucci, M. Anne, Y. Chabre, P. Strobel, J. M. Tarascon and G. Vaughan, *J. Power Sources*, 1999, **81**, 604–606.
52 L. Croguennec, C. Pouillerie, A. N. Mansour and C. Delmas, *J. Mater. Chem.*, 2001, **11**, 131–141.
53 A. Urban, D.-H. Seo and G. Ceder, *npj Comput. Mater.*, 2016, **2**, 16002.
54 J.-P. Peres, *Thesis*, 1996.
55 M. E. A. Y. de Dompablo and G. Ceder, *Chem. Mater.*, 2003, **15**, 63–67.
56 Y. Takahashi, N. Kijima, K. Tokiwa, T. Watanabe and J. Akimoto, *J. Phys.: Condens. Matter*, 2007, **19**, 436202.
57 N. V. Faenza, N. Pereira, D. M. Halat, J. Vinckeviciute, L. Bruce, M. D. Radin, P. Mukherjee, F. Badway, A. Halajko, F. Cosandey, C. P. Grey, A. Van der Ven and G. G. Amatucci, *Chem. Mater.* , 2018, **30**, 7545–7574.
58 Z. Chen, Z. Lu and J. R. Dahn, *J. Electrochem. Soc.*, 2002, **149**, A1604–A1609.

